

# Energy & Environmental Science

Accepted Manuscript



This is an *Accepted Manuscript*, which has been through the Royal Society of Chemistry peer review process and has been accepted for publication.

*Accepted Manuscripts* are published online shortly after acceptance, before technical editing, formatting and proof reading. Using this free service, authors can make their results available to the community, in citable form, before we publish the edited article. We will replace this *Accepted Manuscript* with the edited and formatted *Advance Article* as soon as it is available.

You can find more information about *Accepted Manuscripts* in the [Information for Authors](#).

Please note that technical editing may introduce minor changes to the text and/or graphics, which may alter content. The journal's standard [Terms & Conditions](#) and the [Ethical guidelines](#) still apply. In no event shall the Royal Society of Chemistry be held responsible for any errors or omissions in this *Accepted Manuscript* or any consequences arising from the use of any information it contains.

## ARTICLE

# Extracting Large Photovoltages from a-SiC Photocathodes with an Amorphous TiO<sub>2</sub> Front Surface Field Layer for Solar Hydrogen Evolution

Cite this: DOI: 10.1039/x0xx00000x

Received 00th January 2012,  
Accepted 00th January 2012

DOI: 10.1039/x0xx00000x

[www.rsc.org/](http://www.rsc.org/)Ibadillah A. Digdaya,<sup>a</sup> Lihao Han,<sup>b</sup> Thom W. F. Buijs,<sup>b</sup> Miro Zeman,<sup>b</sup> Bernard Dam,<sup>a</sup> Arno H. M. Smets<sup>b</sup> and Wilson A. Smith<sup>a\*</sup>

**Abstract:** A thin film heterojunction photocathode is fabricated by depositing n-type amorphous titanium dioxide (TiO<sub>2</sub>) onto p-type/intrinsic hydrogenated amorphous silicon carbide (a-SiC). Using this configuration, the photovoltage of the photocathode increases from 0.5 V to 0.8 V under open circuit conditions, indicating the change in band-edge energetics from the semiconductor-liquid junction to the isolated solid p-i-n junction. The p-i-n structure produces an internal electric field that increases the operating photovoltage, and subsequently improves the drift mechanism of photogenerated charge carriers across the intrinsic layer. The enhancement of the photovoltage leads to a very positive photocurrent onset potential of +0.8 V vs. RHE and exhibits a photocurrent density of 8.3 mA cm<sup>-2</sup> at 0 V vs. RHE with only a 100 nm absorber layer. The a-SiC photocathode with a front surface field amorphous TiO<sub>2</sub> layer shows a high stability for 12 hours of operation under photocatalytic conditions. This high performance, very thin, and earth-abundant photocathode is very promising for integration with smaller band gap solar absorbers to form a multijunction system for highly efficient bias-free solar water splitting devices.

## Introduction

Photoelectrochemical (PEC) water splitting has the potential to be a large-scale, sustainable, and efficient route to produce solar fuels (e.g., hydrogen) by harnessing and storing the power of the sun. One of the most attractive features of this technology is that the light absorbing materials can be directly integrated with catalysts to produce a monolithic device, thereby making it more simple and cost-effective than using separate photovoltaic (PV) cells and electrolyzers<sup>1,2</sup>. In order to make this approach competitive with conventional hydrogen production from fossil fuels, i.e., steam-methane reforming, the materials for PEC water splitting need to be made from cheap earth-abundant elements using a low-cost and scalable processing technique.

In recent years, major efforts have focused on single-crystalline silicon (c-Si) based photocathodes<sup>3-10</sup>, due to the natural abundance of Si, its excellent light absorbing and electronic properties and its low-cost and high throughput processing. While these photocathodes show a notably high photocurrent density, a practical device realization with c-Si remains a challenge due to the inability of the narrow band gap of c-Si (i.e., 1.1 eV) to meet the thermodynamic requirements to split water (1.23 V)<sup>11</sup>, plus the necessary overpotentials to drive the reaction<sup>12</sup> (> 0.8 V). A more attractive and realistic

approach to overcome these large potentials is to create a tandem device that contains more than one light absorbing material, which has several benefits such as increased spectral utilization, higher operating voltage, and more flexibility with respect to the band edge positions relative to the water splitting redox potentials<sup>13-16</sup>. Thin film fabrication techniques such as plasma enhanced chemical vapor deposition (PECVD) have the necessary versatility to control the optoelectronic properties of Si and allow for multi-junction devices to be deposited in succession to form homo- and heterojunction films. Therefore, developing thin-film-silicon-based tandem structures with an operating voltage of at least 1.9 V is one of the most attractive and promising approaches to achieve a low-cost bias-free solar water-splitting device.

Hydrogenated amorphous silicon carbide (a-SiC) photocathodes have received a growing interest due to their earth abundant composition, their simple and scalable thin film deposition technique, and their relative high stability in a mildly acidic environment under cathodic bias conditions<sup>17-22</sup>. Moreover, a-SiC has a tunable band gap energy between 1.8 – 2.1 eV<sup>23</sup>, which allows the integration of multi-junction PV cells with smaller band gaps (i.e., 1.1 – 1.8 eV) to form tandem light absorbers for maximum spectral utilization. In our previous work, we have integrated a-SiC photocathodes with thin-film silicon PV junctions (e.g., a-SiC/a-Si/nc-Si) to provide

an additional photovoltage ( $V_{\text{ph}}$ ), resulting in a significant anodic shift of the photocurrent onset potential ( $V_{\text{onset}}$ )<sup>24</sup>. However, low charge carrier collection and slow reaction kinetics at the a-SiC/electrolyte interface limits the overall performance of such triple-junction systems to well below their theoretical limit. The former problem is mainly associated with the a-SiC band edge pinning at the semiconductor-liquid junction (SLJ) and the latter is primarily due to the poor catalytic activity of the photoelectrode for hydrogen evolution.

We herein demonstrate the use of a thin (25 nm) n-type (n) amorphous titanium dioxide ( $\text{TiO}_2$ ) layer grown by atomic layer deposition (ALD) on a p-type/intrinsic (p/i) a-SiC photocathode (110 nm), to create a hetero p-i-n junction. This buried junction significantly increases the  $V_{\text{ph}}$  under photocatalytic conditions which leads to an efficient carrier collection for the water-reduction reaction. This p-i-n configuration also produces the largest reported  $V_{\text{ph}}$  for a-SiC photocathodes, which is mainly due to the improved interfacial electron energetics at the solid/liquid interface. Finally, we place an earth abundant (Ni-Mo) hydrogen evolution catalyst (HEC) on the p-i-n heterojunction photocathode, and report a significant shift in the  $V_{\text{onset}}$  while obtaining  $8.3 \text{ mA cm}^{-2}$  at 0V vs. RHE under AM 1.5 illumination.

## Experimental Section

### Fabrication of a-SiC photocathodes

The a-SiC photocathodes were deposited onto Asahi VU-type substrates using a radio frequency plasma enhanced chemical vapor deposition (RF-PECVD) multi-chamber tool. The substrate was kept at 170 °C during the deposition. The ultrathin boron doped hydrogenated amorphous silicon carbide (a-SiC(B)) was used as the p-type layer (10 nm), decomposed from  $\text{SiH}_4$ ,  $\text{CH}_4$  and  $\text{B}_2\text{H}_6$  diluted  $\text{H}_2$  gas flow under controlled pressure. The thin intrinsic layer (100 nm) was deposited in a separate chamber to avoid cross-contamination. A  $\text{H}_2$  treatment in a low RF power density is followed in the same chamber in order to passivate the p-i interface. After the (p/i) a-SiC thin films were synthesized, a stripe of 300 nm Al was coated on the pre-covered region of the sample as the metal contact using a Provac electron beam evaporator in rotation mode. As the final step, electrical contact was made using a silver wire and graphite paste.

### Atomic layer deposition of $\text{TiO}_2$

Ultrathin amorphous  $\text{TiO}_2$  layers (25 nm) were deposited onto the a-SiC film using a homemade thermal atomic layer deposition (ALD) system. No special treatment was done to pre-clean the a-SiC surface before the  $\text{TiO}_2$  deposition. The  $\text{TiO}_2$  ALD was carried out at a substrate temperature of 150 °C using tetrakis(dimethylamino)titanium, TDMAT and  $\text{H}_2\text{O}$  ( $T_{\text{H}_2\text{O}} = 25 \text{ °C}$ ) as the Ti and O precursors, respectively. The pulsing times are 5 s and 10 ms for Ti and O precursors, respectively. Each precursor was purged for 30 seconds after pulse. The growth rate per cycles measured by ellipsometry was 0.8

Å/cycle. In selected experiments,  $\text{TiO}_2$  films were deposited at different temperatures of 120, 150, 170 and 200 °C.

### Co-catalyst depositions

The Ni-Mo catalyst was deposited by electrodeposition as described previously in other report<sup>10</sup>, only nickel sulfate was used instead of nickel sulfamate. The electrodeposition bath consists of 1.3 M  $\text{Ni}_2\text{SO}_4$ , 0.5 M  $\text{H}_3\text{BO}_3$ , and  $\text{Na}_2\text{MoO}_4$ . No pH adjustment was carried out. The electrodeposition of Ni-Mo catalyst on the photocathodes were performed potentiostatically at -1.5 V vs. Ag/AgCl for the (p/i) a-SiC and at -1.1 V vs. Ag/AgCl for the (p/i) a-SiC/(n)  $\text{TiO}_2$  until 500  $\text{mC/cm}^2$  of charge has passed. During the deposition, the electrodes were shone with the standard AM1.5 illumination (100  $\text{mA cm}^{-2}$ ) using a Newport Sol3A Class AAA solar simulator (type 94023A-SR3) with 450 Watt xenon short arc lamp. Finally, the electrodes were rinsed with milli-Q water before the photoelectrochemical measurements. Pt catalysts were sputter deposited in a PREVAC sputter machine using radio frequency (RF) power at 100 W from a pure Pt target for 18 s, resulting in approximately 1 nm thick Pt islands.

### Photoelectrochemical measurements

The a-SiC photocathodes were photoelectrochemically tested using a potentiostat (EG&G PAR 283) in a three-electrode system, where the a-SiC photocathode with an exposed surface area of 0.283  $\text{cm}^2$  acts as the working electrode, a coiled platinum wire sealed by a fritted-glass tube as the counter electrode and an Ag/AgCl electrode (XR300, saturated KCl and AgCl solution, Radiometer Analytical) as the reference electrode. The electrolyte used was an aqueous 0.5 M potassium hydrogen phthalate (Alfa Aesar, 99.99%) solution (pH 4). Linear sweep voltammetry measurements were done at a scan rate of 50  $\text{mV/s}$  with 25  $\text{mV}$  incremental steps. Photocurrent measurements were performed under simulated AM1.5 solar irradiation (100  $\text{mW cm}^{-2}$ ) using a Newport Sol3A Class AAA solar simulator (type 94023A-SR3) with a 450 Watt xenon short arc lamp. During the measurements, the electrolyte was continuously stirred using a magnetic stirrer and was constantly purged with a mixture of Ar/ $\text{H}_2$  (95/5) to remove oxygen from the solution and to fix the  $\text{H}^+/\text{H}_2$  Nernst potential. All current-potential curves were presented as measured without correction. Monochromatic photocurrent measurements were performed with a 200 W quartz tungsten-halogen lamp coupled with a grating monochromator (Acton SpectraPro 150i). The illumination intensities of the tungsten-halogen lamp were measured using a calibrated photodiode (Ophir PD300-UV). An electronic shutter (Uniblitz LS6) was used, and a long-pass glass filter (Schott) was placed between the monochromator and the sample to remove the second-order diffracted light. The shutter was actuated every 10 seconds, and the photocurrent was taken as the difference between the current when the shutter opened and closed (3 seconds integration time).

### Electrochemical impedance spectroscopy

Electrochemical impedance spectroscopy (EIS) measurements were separately performed on the (p/i) a-SiC electrodes and the amorphous (n) TiO<sub>2</sub> film in the same electrolyte solutions as for the photoelectrochemical testing using potentiostat PARSTAT 4000. The frequency measurement range for all samples was 10 kHz to 1 Hz at a DC potential amplitude of 10 mV. The Mott-Schottky measurements were performed at a fixed frequency of 5 kHz for (p/i) a-SiC and 500 Hz for (n) TiO<sub>2</sub>. The potential was scanned anodically from 0.75 to 0.9 V vs. RHE for a-SiC and cathodically from 0.5 to 0 V vs. RHE for TiO<sub>2</sub>.

## Results and discussion

### a-SiC photocathodes

The (p/i) a-SiC liquid junction photocathode consists of a p-type layer and an intrinsic layer. The diffusion length of the minority carriers in the p-type a-SiC is very short, due to the fact that the defect density in the doped layer is up to three orders of magnitude higher than in the intrinsic layer<sup>25</sup>. Therefore, for our a-SiC photocathode, the p-type layer is designed to be very thin (~10 nm). The main absorber layer of the a-SiC photocathode is the intrinsic (undoped) layer (~100 nm) that is deposited on top of the p-type layer. The p-type layer and the electrolyte set up an internal electric field across the intrinsic layer. Upon illumination, this built-in electric field separates the photogenerated electron-hole pairs and the electrons drift towards the liquid while the holes drift towards the p-type layer. A p-i-n heterojunction photocathode is fabricated by depositing a thin n-type TiO<sub>2</sub> layer (25 nm) onto the (p/i) a-SiC. In this configuration, the electric field across the

intrinsic layer is established by the opposing doped layers, i.e., the (p) a-SiC and the (n) TiO<sub>2</sub>. Under illumination, the photogenerated holes drift to the p-type layer and are collected by the back contact (Fluorine-doped Tin Oxide or FTO), and the photogenerated electrons drift to the n-type layer and are transferred to the electrolyte. A schematic representation and the cross-sectional scanning electron microscope (SEM) image of the (p/i) a-SiC/(n) TiO<sub>2</sub> photocathode are shown in Figure 1a and b, respectively.

### Open-circuit voltage measurements

The PEC performance of a-SiC photocathodes is often limited by the relatively low  $V_{ph}$  of the p-i-liquid junction. The low  $V_{ph}$  of the (p/i) a-SiC originates from the non-ideal band edge positions that are not sufficiently positive relative to the Fermi level pinning at the solid/liquid interface. To eliminate the dependence of the built-in  $V_{ph}$  on the semiconductor-liquid junctions, we introduce a front surface field layer, i.e., an n-type layer, which forms a solid rectifying junction with the (p/i) a-SiC. The p-type and the n-type layer confines the internal electric field across the intrinsic layer that results in a constant  $V_{ph}$  that is independent of the thermodynamic and kinetic properties of the semiconductor-liquid junction. This is an almost identical concept as that of the p-n junction photocathodes which have been described previously in many reports<sup>26,27</sup>. TiO<sub>2</sub> is a well-known n-type material for PEC water splitting and has a high resistance against photo-induced corrosion in aqueous solutions. For this reason, it has been widely used as a protecting layer for unstable photoelectrodes<sup>28–35</sup>. TiO<sub>2</sub> has also been used in conjunction with p-type photocathodes, such as c-Si<sup>36</sup>, Cu<sub>2</sub>O<sup>37,38</sup> and GaP<sup>39</sup>, to form a heterojunction and provide a sufficient internal electric field for photogenerated charge separation. Inspired by this concept, we introduced a thin n-type TiO<sub>2</sub> layer to our (p/i) a-SiC to establish a p-i-n heterojunction photocathode.

Figure 2 shows the change in open-circuit voltage (OCV) in the dark and under illumination conditions, i.e., the  $V_{ph}$  of the (p/i) a-SiC and the (p/i) a-SiC/(n) TiO<sub>2</sub> heterojunction

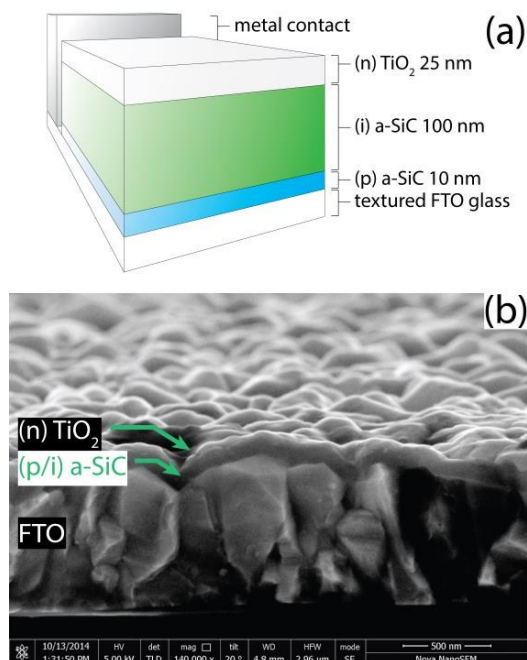


**Figure 1** (a) Schematic structure of the (p/i) a-SiC/(n) TiO<sub>2</sub> photocathode and (b) the cross-sectional SEM image.

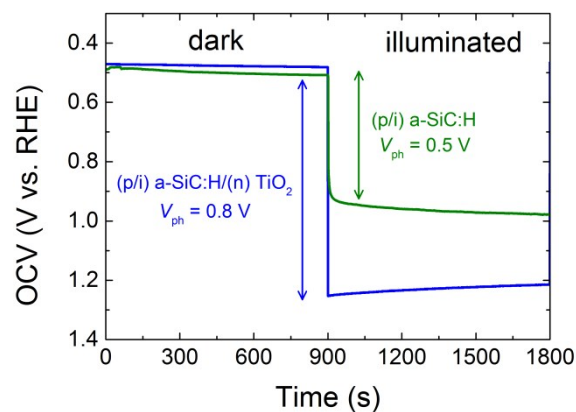


**Figure 2** The change in OCV of (p/i) a-SiC photocathodes with (green) and without the (n) TiO<sub>2</sub> layer (blue). The change in OCV in the dark and under illumination represents the  $V_{ph}$ .

photocathodes. In the dark, both photocathodes show an OCV of  $\sim +0.5$  V vs. RHE, indicating the same equilibrium potential of both photocathodes in the electrolyte solution. Upon illumination, the OCV of the (p/i) a-SiC and the (p/i) a-SiC/(n) TiO<sub>2</sub> drop to  $\sim +1$  V and  $\sim +1.3$  V vs. RHE, respectively. These changes in OCV in the dark and under illumination demonstrate the  $V_{ph}$  of the photocathodes under open-circuit conditions.

To illustrate the interfacial band-edge energetics of the (p/i) a-SiC and the (p/i) a-SiC/(n) TiO<sub>2</sub> photocathodes under open-circuit conditions, the energy band diagrams of the corresponding photocathodes are shown in Figure 3. Before equilibrium in the dark, the conduction and valence bands of the p-type and the intrinsic a-SiC are flat (not shown in the figure) and the valence band edge is positioned at +1 V vs. RHE, corresponding to its flat band potential ( $V_{fb}$ ), as estimated using a Mott-Schottky relationship (ESI, Figure S1). When equilibrium is reached, the Fermi level of the p-type and the intrinsic layers align with the surface electronic state of a-SiC. The existence of surface states originates from the hydroxyl group termination on the oxidized a-SiC surface, that forms an electronic state that is typically situated within the band gap<sup>40–44</sup>. The Fermi level alignment between the p-type layer and the surface state causes a potential difference, i.e., a built-in potential ( $V_{bi}$ ), across the intrinsic layer, as shown in Figure 3a. In the semiconductor-liquid junction system (e.g., p-i-liquid junction), the  $V_{bi}$  is essentially determined by the difference between the valence band edge and the surface state energy level, and sets an upper limit of the maximum achievable  $V_{ph}$ . The Fermi level pinning at the surface state is positioned at +0.5 V vs. RHE, as observed by the OCV measurement in the dark. Upon illumination, the quasi-Fermi levels of the photogenerated electrons and holes split across the intrinsic layer, giving rise to a  $V_{ph}$ , as illustrated in Figure 3b. For the (p/i) a-SiC photocathode, the OCV drops down to +1 V vs. RHE under illumination, which translates to a  $V_{ph}$  of 0.5 V.

Assuming that the band edges are pinned at the interface, this reduces the degree of the band bending of a-SiC, which in turn lead to a nearly flat band condition.

When a thin (n) TiO<sub>2</sub> film is added onto the (p/i) a-SiC, an isolated solid p-i-n junction is created and a new equilibrium is established. The Fermi level of the p-type layer comes into thermal equilibrium with the n-type layer and an internal electric field arises across the intrinsic layer, as shown in Figure 3c. In this solid-state configuration, the  $V_{bi}$  no longer depends on the surface state potential, but primarily on the dopant level of the p-type and the n-type layers. The dopant level of the (p) a-SiC can be varied by controlling the boron concentration during the deposition, and the dopant level of the (n) TiO<sub>2</sub> layer can be tuned during deposition by vacuum in-situ annealing, or post-deposition annealing<sup>29,45</sup>. At the solid/liquid interface, the Fermi level of the (n) TiO<sub>2</sub> equilibrates with the surface state at +0.5 V vs. RHE, which is coincidentally the same surface state energy found previously for the (i) a-SiC. This value is consistent with a study that has been reported previously on TiO<sub>2</sub> grown by ALD<sup>46</sup>. The conduction band edge of TiO<sub>2</sub> at  $-0.1$  V vs. RHE is estimated from the  $V_{fb}$  using the Mott-Schottky analysis with an assumption that the band edges are pinned at the solid/liquid interface. Under illumination, the OCV decreases from +0.5 V to +1.3 V vs. RHE and a  $V_{ph}$  of 0.8 V arises. The change of  $V_{ph}$  from 0.5 V (for the (p/i) a-SiC) to 0.8 V (for the (p/i) a-SiC/(n) TiO<sub>2</sub>) clearly indicates the change in band-edge energetics from a p-i-liquid junction to an isolated p-i-n junction.

### Photoelectrochemical characterization

To evaluate the PEC performance of each photocathode configuration, the current-potential ( $j$ - $V$ ) measurements were performed under simulated Air Mass (AM) 1.5 illumination in a three-electrode system using a potassium hydrogen phthalate

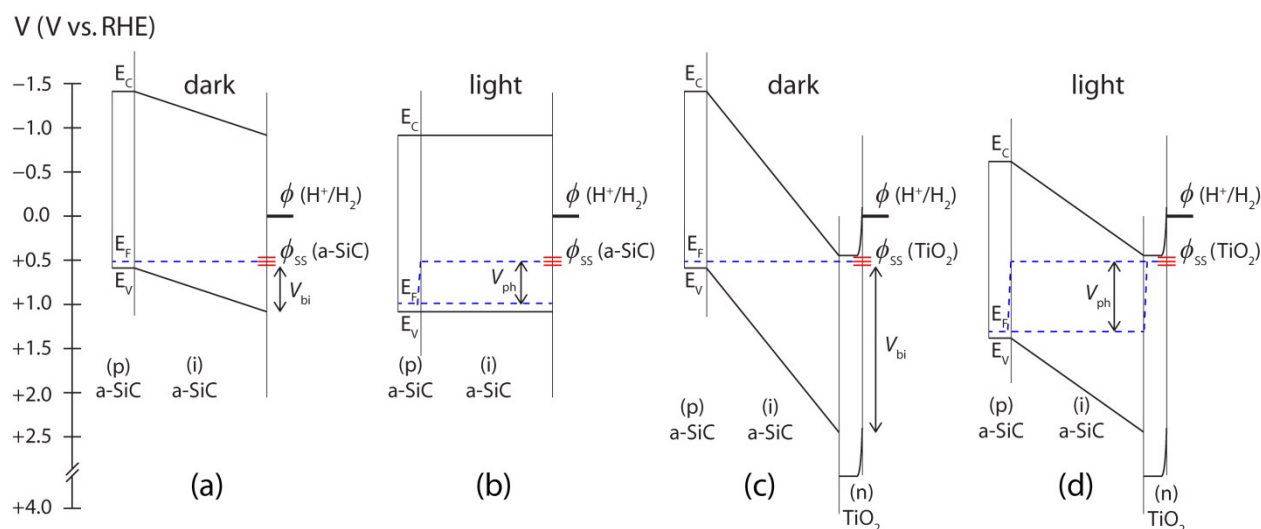


**Figure 3.** The energy band diagram of the (p/i) a-SiC photocathode under open circuit condition: a) in the dark, b) under illumination, and the (p/i) a-SiC/(n) TiO<sub>2</sub> photocathode: c) in the dark, d) under illumination. The band edges are assumed to be pinned at the solid/liquid interface and are estimated using the Mott-Schottky analysis.

electrolyte at pH 4. As shown in Figure 4, the bare (p/i) a-SiC photocathode demonstrates a very poor  $V_{\text{onset}}$  at +0.2 V vs. RHE with a negligible photocurrent density ( $0.15 \text{ mA cm}^{-2}$ ) at the standard  $\text{H}^+/\text{H}_2$  reduction potential of 0 V vs. RHE. The photocurrent does not increase immediately at the  $V_{\text{onset}}$ , indicating the slow reaction kinetics on the semiconductor surface of the uncatalyzed photocathode. When a nickel molybdenum (Ni-Mo) hydrogen evolution co-catalyst is added, the  $V_{\text{onset}}$  anodically shifts to +0.3 V vs. RHE and the photocurrent density increases to  $2.8 \text{ mA cm}^{-2}$  at 0 V vs. RHE (shown in the green curve). Assuming a negligible overpotential of Ni-Mo for the hydrogen evolution reaction, the potential difference between the  $V_{\text{fb}}$  of a-SiC and the  $V_{\text{onset}}$  reflects the minimum thermodynamic potential requirement of the (p/i) a-SiC photocathode to effectively separate photogenerated electrons and holes from each other and therefore to produce photocurrent.

The influence of (n)  $\text{TiO}_2$  on the PEC performance of the (p/i) a-SiC photocathode can also be clearly seen in the  $j$ - $V$  curves in Figure 4. While having sufficiently larger  $V_{\text{ph}}$ , the  $V_{\text{onset}}$  of the (p/i) a-SiC/(n) $\text{TiO}_2$  remains at +0.2 V vs. RHE as that the standard (p/i) a-SiC photocathode. The constant  $V_{\text{onset}}$  with and without  $\text{TiO}_2$  can be attributed to the poor catalytic activity of  $\text{TiO}_2$  surface for the hydrogen evolution reaction in an acidic environment. By adding a Ni-Mo co-catalyst onto the (p/i) a-SiC/(n)  $\text{TiO}_2$  photocathode, the  $V_{\text{onset}}$  significantly shifts to +0.8 V vs. RHE and the photocurrent density drastically increases to  $8.3 \text{ mA cm}^{-2}$  at 0 V vs. RHE. Alternatively, when Pt is used as the co-catalyst, the photocurrent density is slightly higher ( $8.7 \text{ mA cm}^{-2}$ ) at 0 V vs. RHE without any notable shift of  $V_{\text{onset}}$ , thus suggesting a comparable catalytic activity of the earth-abundant Ni-Mo catalyst to the precious metal Pt for the hydrogen evolution reaction.

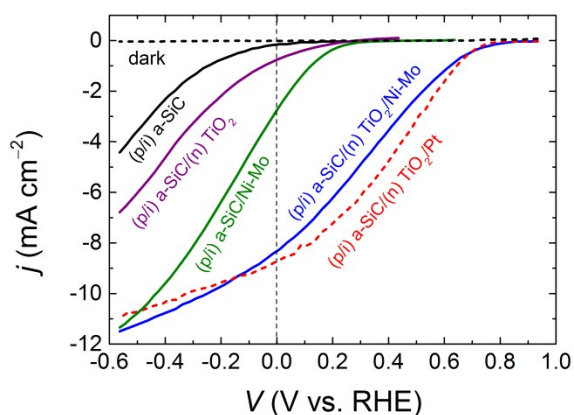


**Figure 4** The  $j$ - $V$  characteristics of the (p/i) a-SiC (black line) and the isolated (p/i) a-SiC/(n)  $\text{TiO}_2$  photocathodes without catalyst (purple line) and with Ni-Mo catalyst (blue line) under the simulated AM1.5 illumination using  $0.5 \text{ M}$  potassium hydrogen phthalate electrolyte solution at pH 4. For comparison, the Pt catalyzed (p/i) a-SiC/(n)  $\text{TiO}_2$  is also shown (red dash line).

### Mott-Schottky analysis

The flat band potential of  $\text{TiO}_2$  is estimated from the Mott-Schottky plot in Figure 5 using EIS. The intersection between

the extrapolated linear line and the x-axis represents the  $V_{\text{fb}}$ , which is approximately  $-0.11 \text{ V}$  vs. RHE. The donor density ( $N_{\text{D}}$ ) of  $\text{TiO}_2$  can be determined using Mott-Schottky relationship in Equation (1)<sup>47</sup>:

$$\frac{1}{C^2} = \frac{2}{\epsilon_0 \epsilon_r N_{\text{D}}} \left( V - V_{\text{fb}} - \frac{kT}{e} \right) \quad (1)$$

where  $C$  is the capacitance density,  $e$  is the elementary charge,  $\epsilon_0$  is the permittivity in vacuum,  $\epsilon_r$  is the relative permittivity of  $\text{TiO}_2$  (75)<sup>48</sup>,  $k$  is Boltzmann's constant and  $T$  the temperature (298 K). The exposed area of the photocathode in this experiment was  $0.28 \text{ cm}^2$ . The donor density of ALD  $\text{TiO}_2$  deposited at  $150 \text{ }^\circ\text{C}$  is  $1.56 \times 10^{20} \text{ cm}^{-3}$ . The position of the Fermi level ( $E_{\text{F}}$ ) relative to the conduction band ( $E_{\text{CB}}$ ) is approximated using the relationship in Equation (2) and (3):

$$E_{\text{CB}} - E_{\text{F}} = \frac{kT}{e} \ln \left( \frac{N_{\text{C}}}{N_{\text{D}}} \right) \quad (2)$$

$$N_{\text{C}} = 2 \left( \frac{2\pi m_e^* kT}{h^2} \right)^{3/2} \quad (3)$$

where  $h$  is Planck's constant,  $m_e^*$  is the effective mass of the electron, and  $N_{\text{C}}$  is the effective density of states in the conduction band. In this equation,  $N_{\text{C}}$  is calculated using the assumption that the  $m_e^*$  of amorphous  $\text{TiO}_2$  is the same as that the anatase  $\text{TiO}_2$  ( $10 m_0$ )<sup>49</sup>. These relationships suggest that the Fermi level is positioned  $41.44 \text{ mV}$  below the conduction band.

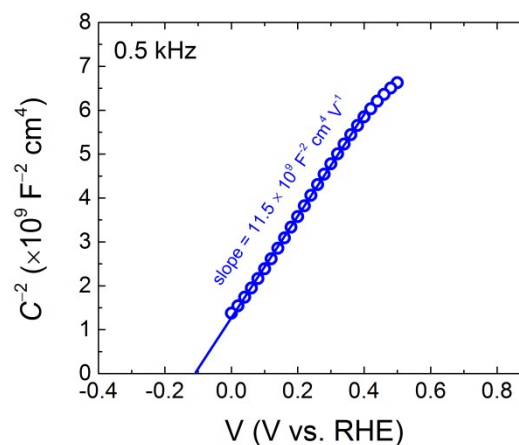


**Figure 5** Mott-Schottky plot of  $\text{TiO}_2$  film deposited on FTO at  $150 \text{ }^\circ\text{C}$  measured using the electrochemical impedance spectroscopy at a frequency of  $500 \text{ Hz}$ . The intersection of the extrapolated linear line with the x-axis represents the  $V_{\text{fb}}$ . The measurement was performed using the same electrolyte as that for photoelectrochemical measurement ( $0.5 \text{ M}$  potassium hydrogen phthalate at pH 4)

To further understand the origin of the  $V_{\text{onset}}$ , energy band diagrams of the illuminated (p/i) a-SiC/(n)  $\text{TiO}_2$  photocathodes are illustrated in more detail in Figure 6. It is important to note that the Ni-Mo co-catalyst we deposited on the photocathode surface is in the form of nanoparticle (ESI, Figure S11) and the

1 nm thick Pt catalyst is in the form of metal island<sup>50</sup>. Thus the front TiO<sub>2</sub> layer is still in contact with water and forming a semiconductor-liquid junction, which is represented by the band bending of TiO<sub>2</sub> near the interface. As shown previously in Figure 4, the  $V_{\text{onset}}$  of the (p/i) a-SiC/(n) TiO<sub>2</sub> photocathode with either Ni-Mo or the Pt co-catalyst is +0.8 V vs. RHE, which is more negative than the OCV under illumination (+1.3 V vs. RHE). The absence of  $V_{\text{onset}}$  under open circuit conditions and illumination can be explained by the interfacial energetics of electrons relative to the H<sup>+</sup>/H<sub>2</sub> redox energy level as shown in Figure 6a. At an applied potential of +1.3 V vs. RHE, the  $V_{\text{ph}}$  sets the conduction band of the (n) TiO<sub>2</sub> slightly more negative than the quasi-Fermi level of the photogenerated electrons (+0.5 V vs. RHE). Due to the large difference of energy levels between the conduction band of the (n) TiO<sub>2</sub> and the H<sup>+</sup>/H<sub>2</sub> reduction potential, the electrons do not have sufficient energy to overcome the high energy barrier, and as a result they recombine before getting injected to the electrolyte. It is worth emphasizing that isolating the solid-state junction from the electrolyte leads to an internal electric field confinement that is independent on the applied external bias<sup>26,27</sup>. This implies that the  $V_{\text{ph}}$  of our p-i-n junction photocathode remains constant at any applied potential. When the potential is cathodically increased to +0.8 V vs. RHE, the  $V_{\text{ph}}$  sets the conduction band of the (n) TiO<sub>2</sub> more negative than the H<sup>+</sup>/H<sub>2</sub> reduction potential, thereby allowing the electrons to transfer, or tunnel through the depletion layer barrier to the electrolyte (Figure 6b). This reasoning clearly explains the  $V_{\text{onset}}$  of +0.8 V vs. RHE for these experimental conditions.

To understand the electron transfer mechanism from the conduction band to the electrolyte, it is vitally important to approximate the depletion layer width ( $W_D$ ) of TiO<sub>2</sub>. This can be calculated using the data obtained from the Mott-Schottky results using Equation (4):

$$W_D = \left[ \frac{2\epsilon_0\epsilon_r}{eN_D} \left( V - V_{\text{fb}} - \frac{kT}{e} \right) \right]^{1/2} \quad (4)$$

From Equation (4), it is clear that the width of the depletion region is a function of the applied potential ( $V$ ). Therefore, increasing the potential towards the  $V_{\text{fb}}$  will shorten the depletion layer width. Although a potential barrier still exists due to conduction band-edge pinning at -0.1 V vs. RHE, electrons are still likely to be able to transfer from the conduction band to the electrolyte. This is due to the fact that when the electron quasi-Fermi level of TiO<sub>2</sub> is positioned at 0 V vs. RHE, the depletion region width of the amorphous TiO<sub>2</sub> becomes sufficiently small (2 nm) so that the electrons can still tunnel through this small barrier. Seger *et al.* reported that TiO<sub>2</sub> with a depletion layer width of a few nanometers and sufficiently negative  $V_{\text{fb}}$  still allowed electrons to tunnel at oxidative potentials<sup>45</sup>. This likely means that the width of the depletion layer barrier played a more crucial role than the height of the potential barrier in determining electron tunnelling.

#### Photoresponse characterization

The photoelectrochemical performance of the a-SiC photocathodes were further characterized by measuring the incident-photon-to-current efficiency (IPCE) at an applied potential of 0 V vs. RHE, as shown in Figure 7. The low IPCE in the ultraviolet (UV) region accounts for the parasitic absorption by the FTO and the p-type layer that does not contribute to photocurrent generation, while the decline of IPCE in the near-infrared (NIR) region corresponds to the band gap limitation of the a-SiC. It is important to note that the band gap of a-SiC used in this study is ~2.0 eV (ESI, Figure S3), corresponding to an absorption edge at 620 nm. The extended

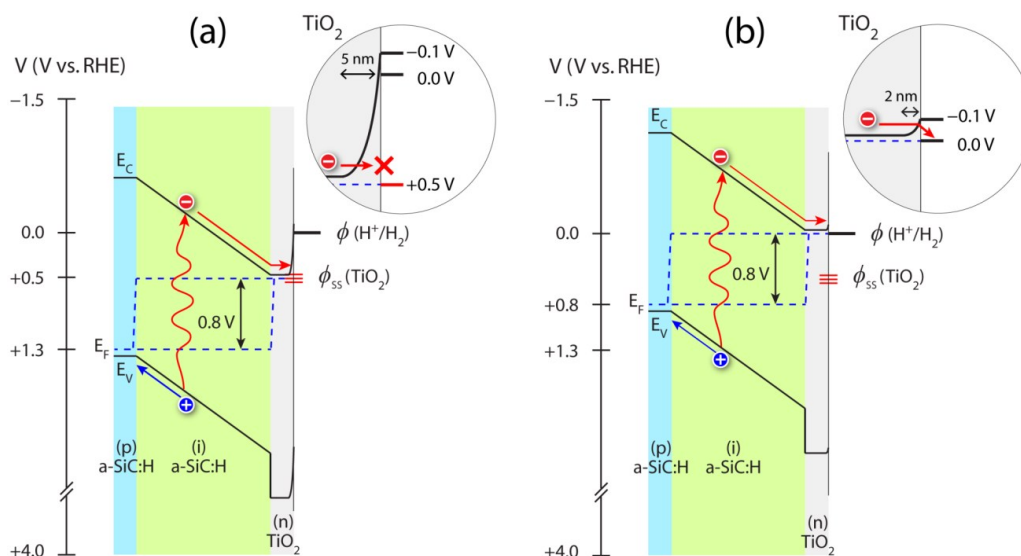


**Figure 6** Energy band diagram of the (p/i) a-SiC/(n) TiO<sub>2</sub> photocathode (a) at an applied potential +1.3 V vs. RHE, corresponding to the OCV under illumination, and (b) under bias at +0.8 V vs. RHE, corresponding to the  $V_{\text{onset}}$ . The catalysts (Ni-Mo or Pt) are not shown in the figure since TiO<sub>2</sub> still interact with electrolyte, and therefore they do not influence the band-edge energetics.

spectral response up to 700 nm is ascribed to absorption due to transitions between band tail states whose energy distributions are increased with carbon incorporation<sup>51</sup>. In addition, light scattering by the rough surface of the textured FTO substrate (Asahi VU-type) increases the optical path length and hence enhances the light absorption, particularly the weakly absorbed light at long wavelengths. The predicted solar photocurrent using the American Society for Testing and Materials AM1.5 global (ASTM AM1.5G) spectrum<sup>52</sup> of the Ni-Mo catalyzed (p/i) a-SiC photocathode reveals a value of  $2.9 \text{ mA cm}^{-2}$  (details are provided in ESI, Figure S4), which is almost consistent to the photocurrent previously shown in Figure 4 (i.e.,  $2.8 \text{ mA cm}^{-2}$ ). This minor deviation is primarily due to the mismatch of spectral irradiance between our solar simulator and the ASTM AM1.5G (ESI, Figure S5). Throughout the entire spectrum, the Ni-Mo catalyzed (p/i) a-SiC/(n) TiO<sub>2</sub> photocathode demonstrates a much higher IPCE than the standard (p/i) a-SiC photocathode and yields a quantum efficiency peak of 63% at 460 nm. Using the ASTM AM1.5 G spectrum, the predicted solar photocurrent shows nearly absolute agreement of  $8.5 \text{ mA cm}^{-2}$  with the photocurrent measured by our solar simulator (i.e.,  $8.3 \text{ mA cm}^{-2}$ ).

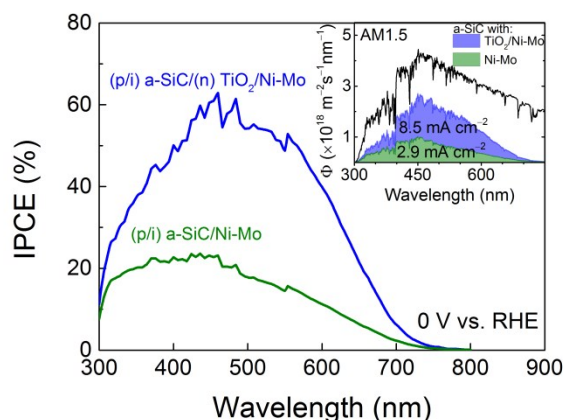


**Figure 7** The IPCE of the standard (p/i) a-SiC and the (p/i) a-SiC/(n) TiO<sub>2</sub> photocathodes with Ni-Mo catalysts measured at 0 V vs. RHE. The shaded areas under the curves shown in the inset are the converted photon fluxes and are derived from the multiplication of IPCE of both photocathodes and the photon flux of the ASTM AM1.5G spectrum. The predicted solar photocurrents of both photocathodes shown in the inset are calculated by integrating the product of IPCE and the spectral irradiance of the ASTM AM1.5G over the spectrum.

### Stability measurement

The stability of both Ni-Mo catalyzed (p/i) a-SiC and the (p/i) a-SiC/(n) TiO<sub>2</sub> photocathodes were evaluated for 12 hours of operation at an applied potential of 0 V vs. RHE, and are shown in Figure 8. Without TiO<sub>2</sub> the photocurrent of the (p/i) a-SiC photocathode drastically dropped to only 20% of its initial value. The decay of photocurrent is most likely associated with the detachment of the Ni-Mo catalyst due to its poor adhesion on the a-SiC surface that causes a decrease of catalytic activity. When the Ni-Mo was redeposited, the photocurrent could be restored as its initial value without any change in the  $V_{\text{onset}}$  (ESI, Figure S6).

The Ni-Mo coated (p/i) a-SiC/(n) TiO<sub>2</sub> shows a high stability without noticeable degradation of photocurrent during a 12 hour measurement at an applied potential of 0 V vs. RHE, as shown in Figure 8. The increase of the photocurrent within the first two hours may be ascribed to TiO<sub>2</sub> surface etching under cathodic conditions. It is worth to mention that applying a potential bias at 0 V vs. RHE will pin the conduction band of TiO<sub>2</sub> approximately 0.8 V more negative than the  $V_{\text{fb}}$ , which subsequently leads to a strong band bending of TiO<sub>2</sub> near the interface. Several studies have shown that the application of a bias at potentials more reductive than the  $V_{\text{fb}}$  can lead to electron accumulation at the TiO<sub>2</sub> surface that can promote the proton-assisted reduction process of Ti<sup>4+</sup> to Ti<sup>3+</sup>, which is usually accompanied with an insignificant rate of hydrogen evolution<sup>28,53</sup>. Thus the observed photocurrent may predominantly correspond to the reduction of titania film rather than water. However, it can be argued that a fast electron transfer from the semiconductor to electrolyte by the application of an efficient hydrogen evolution co-catalyst will prevent the detrimental effect of electron trapping at the TiO<sub>2</sub> surface<sup>54</sup>. The Ni-Mo catalyst exhibits a similar catalytic activity to Pt with no substantial difference in the photocurrent density and the  $V_{\text{onset}}$ , as previously evidenced by the  $j$ - $V$  curves of the catalyzed (p/i) a-SiC/(n) TiO<sub>2</sub> photocathodes in Figure 4. Hence, the observed photocurrent within the 12 hour measurement can be assigned to hydrogen generation with Faradaic efficiency of nearly 100%. Although the experiment was not continued further, the 12 hour stability measurement demonstrates the beneficial properties of TiO<sub>2</sub>, not only as an n-type front surface field layer, but also as an adhesive layer for co-catalysts and an interfacial protecting layer against corrosion in aqueous solutions under cathodic conditions. Many reports have shown that TiO<sub>2</sub> and Ni-Mo catalysts are highly stable in acidic and alkaline media within the course of days and even months<sup>28–39</sup>.

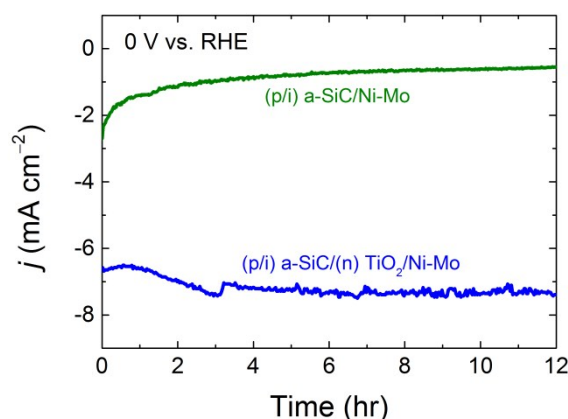


**Figure 8** The chronoamperometry measurement of the Ni-Mo coated (p/i) a-SiC and (p/i) a-SiC/(n) TiO<sub>2</sub> photocathodes for 12 hours under the simulated AM1.5 illumination. During the measurement, the potential was held at 0 V vs. RHE. All samples were measured in 0.5 M potassium hydrogen phthalate electrolyte solution at pH 4.

While showing a notable photocurrent density of  $8.3 \text{ mA cm}^{-2}$  at the  $\text{H}^+/\text{H}_2$  reduction potential, the  $V_{\text{onset}}$  of  $+0.8 \text{ V}$  vs. RHE, however, still does not satisfy the thermodynamic potential requirement potential for water splitting. Nevertheless, considering the absorption edge of  $700 \text{ nm}$  and the total thickness of our (p/i) a-SiC/(n)  $\text{TiO}_2/\text{Ni-Mo}$  photocathode which is approximately only  $150 \text{ nm}$ , this opens up the possibility to use a second (or third) absorber material for the utilization of longer wavelength light in a tandem photocathode configuration or in a dual photoelectrode system (e.g., photocathode and photoanode) to provide additional  $V_{\text{ph}}$ . To give an illustration, assuming there is no limitation on the photocurrent due to light shading and series connection of multi-junction system, the integration with a micromorph (a-Si/nc-Si) PV will give an extra  $\sim +1.2 \text{ V}$  to the initial  $V_{\text{onset}}$ <sup>24</sup>. Additionally, by using an efficient oxygen evolution catalyst as the counter electrode, a benchmark of 10% solar-to-hydrogen (STH) efficiency PEC water-splitting device can be achieved using thin film Si-based photoelectrodes.

## Conclusion

In summary we have investigated the change in the interfacial energetics of the semiconductor-liquid junction belonging to a (p/i) a-SiC photocathode by adding a thin (n)  $\text{TiO}_2$  layer to form a hetero p-i-n junction. The  $V_{\text{onset}}$  of the catalyzed (p/i) a-SiC/(n)  $\text{TiO}_2$  photocathode anodically shifts from  $+0.3 \text{ V}$  to  $+0.8 \text{ V}$  vs. RHE. The (p/i) a-SiC/ $\text{TiO}_2$  shows a photocurrent density of  $8.3 \text{ mA cm}^{-2}$  with a Ni-Mo catalyst and  $8.7 \text{ mA cm}^{-2}$  with a Pt catalyst, which is markedly higher than the initial (p/i) a-SiC ( $0.15 \text{ mA cm}^{-2}$ ) at the standard  $\text{H}^+/\text{H}_2$  reduction potential. Using Mott-Schottky analysis, the conduction band edge position and the electronic properties of the (n)  $\text{TiO}_2$  can be estimated, which helps to verify the electron transfer mechanism through the conduction band. The spectral response reveals a dramatic increase throughout the spectrum upon the addition of the (n)  $\text{TiO}_2$  onto the (p/i) a-SiC, indicating a higher conversion of light to photocurrent within the same spectral range. We finally showed that the  $25 \text{ nm}$  thick ALD  $\text{TiO}_2$  coupled with a Ni-Mo catalyst was stable and able to maintain the durability of the a-SiC photocathode, as suggested by the 12 hours stability measurement under PEC operating conditions. This experimental study also suggests that  $\text{TiO}_2$  can be used as the n-type layer for heterojunction thin-film-Si-based photoelectrodes.

## Acknowledgments

The authors would like to thank Joost Middelkoop from MECS group at TU Delft for the assistance with atomic layer depositions, Ming Ma from MECS group at TU Delft for the assistance with the Pt sputter deposition and Carel Heerkens from Charged Particle Optics group at TU Delft for the assistance with SEM images. This work is part of the research programme of the Foundation for Fundamental Research on Matter (FOM), which is part of the Netherlands Organisation

for Scientific Research (NWO) and is financed in part by the BioSolar Cells open innovation consortium (W.A. Smith and I.A. Digdaya), supported by the Dutch Ministry of Economic Affairs, Agriculture and Innovation. Financial support from the VIDI project (granted to Dr. A.H.M. Smets and L. Han) by NWO-STW is gratefully acknowledged.

## Notes and references

a Materials for Energy Conversion and Storage (MECS), Department of Chemical Engineering Delft University of Technology, P.O. Box 5045, Delft 2600 GA, The Netherlands. E-mail: w.a.smith@tudelft.nl.

b Photovoltaic Materials and Devices (PVMD), Department of Electrical Sustainable Energy, Delft University of Technology, P.O. Box 5031, Delft 2600 GA, The Netherlands.

† Electronic Supplementary Information (ESI) available. See DOI: 10.1039/b000000x/

1. R. Sathre, C. D. Scown, W. R. Morrow, J. C. Stevens, I. D. Sharp, J. W. Ager, K. Walczak, F. a. Houle and J. B. Greenblatt, *Energy & Environmental Science*, 2014, **7**.
2. T. J. Jacobsson, V. Fjällström, M. Edoff and T. Edvinsson, *Energy & Environmental Science*, 2014, **7**, 2056.
3. D. V Esposito, I. Levin, T. P. Moffat and a A. Talin, *Nature materials*, 2013, **12**, 562–8.
4. J. Oh, T. G. Deutsch, H.-C. Yuan and H. M. Branz, *Energy & Environmental Science*, 2011, **4**, 1690.
5. Y. Hou, B. L. Abrams, P. C. K. Vesborg, M. E. Björketun, K. Herbst, L. Bech, A. M. Setti, C. D. Damsgaard, T. Pedersen, O. Hansen, J. Rossmeisl, S. Dahl, J. K. Nørskov and I. Chorkendorff, *Nature materials*, 2011, **10**, 434–8.
6. U. Sim, H.-Y. Jeong, T.-Y. Yang and K. T. Nam, *Journal of Materials Chemistry A*, 2013, **1**, 5414.
7. U. Sim, T.-Y. Yang, J. Moon, J. An, J. Hwang, J.-H. Seo, J. Lee, K. Y. Kim, J. Lee, S. Han, B. H. Hong and K. T. Nam, *Energy & Environmental Science*, 2013, **6**, 3658.
8. S. W. Boettcher, J. M. Spurgeon, M. C. Putnam, E. L. Warren, D. B. Turner-Evans, M. D. Kelzenberg, J. R. Maiolo, H. a Atwater and N. S. Lewis, *Science (New York, N.Y.)*, 2010, **327**, 185–7.
9. E. L. Warren, J. R. McKone, H. a. Atwater, H. B. Gray and N. S. Lewis, *Energy & Environmental Science*, 2012, **5**, 9653.
10. J. R. McKone, E. L. Warren, M. J. Bierman, S. W. Boettcher, B. S. Brunschwig, N. S. Lewis and H. B. Gray, *Energy & Environmental Science*, 2011, **4**, 3573.
11. R. van de Krol and M. Grätzel, *Photoelectrochemical Hydrogen Production*, Springer US, Boston, MA, 2012, vol. 102.
12. M. T. M. Koper, *Journal of Electroanalytical Chemistry*, 2011, **660**, 254–260.
13. J. R. Bolton, S. J. Strickler and J. S. Connolly, *Nature*, 1985, **316**, 495–500.
14. J. Brillet, J. Yum, M. Cornuz and T. Hisatomi, *Nature Photonics*, 2012, **6**.
15. S. Hu, C. Xiang, S. Haussener, A. D. Berger and N. S. Lewis, *Energy & Environmental Science*, 2013, **6**, 2984.
16. H. Döscher, J. F. Geisz, T. G. Deutsch and J. a. Turner, *Energy & Environmental Science*, 2014, **7**, 2951.

17. J. Hu, F. Zhe, I. Matulionis, K. Augusto, T. Deutsch, E. Miller and A. Madan, in *23rd European Photovoltaic Solar Energy Conference and Exhibition*, 2008, pp. 69–72.
18. F. Zhu, J. Hu, I. Matulionis, T. Deutsch, N. Gaillard, A. Kunrath, E. Miller and A. Madan, *Philosophical Magazine*, 2009, **89**, 2723–2739.
19. F. Zhu, J. Hu, I. Matulionis, T. Deutsch, N. Gaillard, E. Miller and A. Madan, in *Solar Power*, ed. R. D. Rugescu, InTech, 2012.
20. I. Matulionis, F. Zhu, J. Hu, T. Deutsch, A. Kunrath, E. Miller, B. Marsen and A. Madan, in *Solar Hydrogen and Nanotechnology II, Proc. of SPIE*, ed. G. Westin, 2008, vol. 7044, p. 70440D–70440D–8.
21. F. Zhu, J. Hu, A. Kunrath, I. Matulionis, B. Marsen, B. Cole, E. Miller and A. Madan, in *Solar Hydrogen and Nanotechnology II, Proc. of SPIE*, ed. J. Guo, 2007, vol. 6650, p. 66500S–66500S–9.
22. I. Matulionis, J. Hu, F. Zhu, J. Gallon, N. Gaillard, T. Deutsch, E. Miller and A. Madan, in *Solar Hydrogen and Nanotechnology II, Proc. of SPIE*, eds. H. Idriss and H. Wang, 2010, vol. 7770, p. 77700Z–77700Z–8.
23. A. Madan and M. Shaw, *The physics and applications of amorphous semiconductors*, 1988.
24. L. Han, I. A. Digdaya, T. W. F. Buijs, F. F. Abdi, Z. Huang, R. Liu, B. Dam, M. Zeman, W. a. Smith and A. H. M. Smets, *J. Mater. Chem. A*, 2014, **00**, 1–8.
25. M. Zeman, in *Thin Film Solar Cells Fabrication, Characterization and Applications*, eds. J. Poortmans and V. Arkhipov, John Wiley & Sons, Ltd, Chichester, 2006, pp. 173–236.
26. E. L. Warren, S. W. Boettcher, M. G. Walter, H. A. Atwater and N. S. Lewis, *The Journal of Physical Chemistry C*, 2011, **115**, 594–598.
27. S. W. Boettcher, E. L. Warren, M. C. Putnam, E. A. Santori, D. Turner-Evans, M. D. Kelzenberg, M. G. Walter, J. R. McKone, B. S. Brunschwig, H. A. Atwater and N. S. Lewis, *Journal of the American Chemical Society*, 2011, **133**, 1216–9.
28. A. Paracchino, V. Laporte, K. Sivula, M. Grätzel and E. Thimsen, *Nature materials*, 2011, **10**, 456–61.
29. B. Seger, T. Pedersen, A. B. Laursen, P. C. K. Vesborg, O. Hansen and I. Chorkendorff, *Journal of the American Chemical Society*, 2013, **135**, 1057–64.
30. Y. Lin, C. Battaglia, M. Boccard, M. Hettick, Z. Yu, C. Ballif, J. W. Ager and A. Javey, *Nano letters*, 2013, **13**, 5615–8.
31. Y. W. Chen, J. D. Prange, S. Dühnen, Y. Park, M. Gunji, C. E. D. Chidsey and P. C. McIntyre, *Nature materials*, 2011, **10**, 539–44.
32. S. Hu, M. R. Shaner, J. A. Beardslee, M. Lichterman, B. S. Brunschwig and N. S. Lewis, *Science (New York, N.Y.)*, 2014, **344**, 1005–9.
33. M. T. McDowell, M. F. Lichterman, J. M. Spurgeon, S. Hu, I. D. Sharp, B. S. Brunschwig and N. S. Lewis, *The Journal of Physical Chemistry C*, 2014, **118**, 19618–19624.
34. M. F. Lichterman, A. I. Carim, M. T. McDowell, S. Hu, H. Gray, B. S. Brunschwig and N. S. Lewis, *Energy & Environmental Science*, 2014, **7**, 3334–3337.
35. C. G. Morales-Guio, S. D. Tilley, H. Vrubel, M. Grätzel and X. Hu, *Nature communications*, 2014, **5**, 3059.
36. Y. J. Hwang, A. Boukai and P. Yang, *Nano letters*, 2008, **3**, 1–6.
37. W. Siripala, A. Ivanovskaya, T. F. Jaramillo, S. Baeck and E. W. McFarland, *Solar Energy Materials and Solar Cells*, 2003, **77**, 229–237.
38. M. Wang, L. Sun, Z. Lin, J. Cai, K. Xie and C. Lin, *Energy & Environmental Science*, 2013, **6**, 1211.
39. M. Malizia, B. Seger, I. Chorkendorff and P. C. K. Vesborg, *Journal of Materials Chemistry A*, 2014, **2**, 6847.
40. S. Dhar, O. Seitz, M. D. Halls, S. Choi, Y. J. Chabal and L. C. Feldman, *Journal of the American Chemical Society*, 2009, **131**, 16808–13.
41. W. M. Ayers, *Journal of Applied Physics*, 1982, **53**, 6911.
42. Y. K. Chan and T. S. Jayadevaiah, *Journal of Non-Crystalline Solids*, 1973, **12**, 314–320.
43. J. Chazalviel, *Porous Silicon Science and Technology*, 1995.
44. S. Weisz, J. Avalos, M. Gomez and A. Many, *Surface science*, 1995, **6028**.
45. B. Seger, S. D. Tilley, T. Pedersen, P. C. K. Vesborg, O. Hansen, M. Grätzel and I. Chorkendorff, *Journal of Materials Chemistry A*, 2013, **1**, 15089.
46. C. Du, M. Zhang, J.-W. Jang, Y. Liu, G.-Y. Liu and D. Wang, *The Journal of Physical Chemistry C*, 2014, **118**, 17054–17059.
47. K. Gelderman, L. Lee and S. W. Donne, *Journal of Chemical Education*, 2007, **84**, 685.
48. D. M. King, X. Du, A. S. Cavanagh and A. W. Weimer, *Nanotechnology*, 2008, **19**, 445401.
49. B. Enright and D. Fitzmaurice, *The Journal of Physical Chemistry*, 1996, **100**, 1027–1035.
50. M. Miyauchi, *Physical chemistry chemical physics : PCCP*, 2008, **10**, 6258–65.
51. P. A. Bayley and J. M. Marshall, *Philosophical Magazine Part B*, 1996, **73**, 429–444.
52. American Society for Testing and Materials (ASTM), <http://rredc.nrel.gov/solar/spectra/am1.5/>.
53. H. Pelouchova, P. Janda, J. Weber and L. Kavan, *Journal of Electroanalytical Chemistry*, 2004, **566**, 73–83.
54. S. D. Tilley, M. Schreier, J. Azevedo, M. Stefik and M. Graetzel, *Advanced Functional Materials*, 2014, **24**, 303–311.